PAPER

Check for updates

Synergistic effect of modified pore and heterojunction of MOF-derived α-Fe₂O₃/ZnO for superior photocatalytic degradation of methylene blue

Liyana Labiba Zulfa,[a] Ratna Ediati, [ID] *[a] Alvin Romadhoni Putra Hidayat,[a] Riki Subagyo,[a] Nuhaa Faaizatunnisa,[a] Yuly Kusumawati,[a] Djoko Hartanto,[a] Nurul Widiastuti, [ID] [a] Wahyu Prasetyo Utomo[ab] and Mardi Santoso [ID] [a]

Mesoporous heterojunction MOF-derived α-Fe₂O₃/ZnO composites were prepared by a simple calcination of α-Fe₂O₃/ZIF-8 as a sacrificial template. The optical properties confirm that coupling of both the modified pore and the n–n heterojunction effectively reduces the possibility of photoinduced charge carrier recombination under irradiation. The mesoporous Fe(25)ZnO with 25% loading of α-Fe₂O₃ exhibited the best performance in MB degradation, up to ~100% after 150 minutes irradiation, higher than that of pristine ZnO and α-Fe₂O₃. Furthermore, after three cycles reusability, mesoporous Fe(25)ZnO still showed an excellent stability performance of up to 95.42% for degradation of MB. The proposed photocatalytic mechanism of mesoporous Fe(25)ZnO for the degradation of MB corresponds to the n–n heterojunction system. This study provides a valuable reference for preparing mesoporous MOF-derived metal oxides with an n–n heterojunction system to enhance MB photodegradation.

Introduction

The drastic increase in the concentration of azo dyes in the aquatic environment due to increased industrial activity has become an aquatic environmental problem that needs to be addressed. There are several methods for removing dye contaminants, including adsorption, microbial degradation, membrane filtration and photocatalysis. Photocatalysis is part of the advanced oxidation process (AOP) which has advantages over other methods such as (i) reducing the use of chemicals (ii) generating free radicals such as hydroxyl radicals ($^{\bullet}$OH) involved in the destructive mineralization of water-soluble organic–inorganic pollutants and (iii) avoiding secondary waste.[1–3] Semiconductors are widely used as photocatalysts because they have the ability to convert solar energy into chemical energy *via* redox reactions.[4] Theoretically, the redox process of the photogeneration carrier depends on the values of the conduction band (CB) and the valence band (VB). The CB potential (E_{CB}) must be more negative than the $O_2/^{\bullet}O_2$ reduction potential to generate hydroxide radicals and the VB potential (E_{VB}) must be

more positive than the $H_2O/^{\bullet}OH$ oxidation potential to generate superoxide radicals.[5]

Zinc oxide (ZnO) is an n-type semiconductor with a large band gap (3.2–3.5 eV), lower toxicity and high physicochemical stability.[6,7] Moreover, ZnO is popular in photocatalytic field due to its high charge carrier mobility, high performance and low exciton binding.[8] However, there are some drawbacks of ZnO such as fast carrier recombination rate, low quantum yield efficiency, and lower separation charge transfer.[9,10] Moreover, morphology, surface area and pore size distribution are still the main obstacles to ZnO as a photocatalyst. Comparing the performance of semiconductors with bulky and porous structures, it has been reported in previous studies that bulky structures cause volume recombination that will reduce the performance or inactivity of the semiconductor. These results indicate that semiconductors with porous structures have better photocatalytic performance than semiconductors with bulky structures.[11,12] Therefore, it is a great effort to produce semiconductors with porous structures to improve the efficiency of charge carriers, to develop new photocatalyst by extending the absorption wavelength, and to develop new synthesis methods to increase the surface area and pore size.

To date, several studies have been reported to improve photocatalytic activity through the development of heterojunction systems.[13] The heterojunction system can improve the light sensitivity of the semiconductor, leading to higher

[a]Department of Chemistry, Faculty of Science, Institut Teknologi Sepuluh Nopember, Surabaya 60111, Indonesia. E-mail: rediati@chem.its.ac.id
[b]School of Energy and Environment, City University of Hong Kong, Hong Kong 999077, China

absorption and energy conversion efficiency of photons, suppressing electron recombination and charge carrier separation more effectively than a single semiconductor.[14–16] The fabrication of heterojunction with a matching bandgap is an effective strategy to produce new high quality photocatalysts. Lei et al., reported that the heterojunction between α-Fe$_2$O$_3$ and SnO$_2$ showed better performance for MB degradation compared to α-Fe$_2$O$_3$ and pure SnO$_2$.[17] In another study, Bouziani et al., reported that the heterojunction between α-Fe$_2$O$_3$ and TiO$_2$ performed better for MB degradation than the original. Pure TiO$_2$ has a photocatalytic performance of 30%, after addition of α-Fe$_2$O$_3$ the photocatalytic performance increases to 92% in 160 minutes.[18] Therefore, improving the performance of a semiconductor can be done by increasing its porosity.

Metal–organic framework (MOF) is a type of porous material composed of a metal and a ligand with coordination bonds, also known as a porous coordination polymer (PCPy). The adjustable pore size and unique structure of the MOF provide new insights for the preparation of MOF-derived metal oxides.[19,20] Unlike other metal oxide precursors, MOFs as metal oxide template offer broad options in the design and fabrication of hierarchical porous structures, abundant active sites, and large surface area. For example, the TiO$_2$/ZrO$_2$ composite made from the Ti/Zr bimetallic MOF showed a high degradation performance toward organic compounds, of up to 86.3% after 120 minutes of irradiation.[21–25] When MOFs are heated in air, the ligands decompose into gases such as COx and NOx, while free metals react with oxygen to form porous metal oxides. ZIF-8 is one of the zinc-based MOFs that has been widely used as a self-sacrificial template for porous metal oxides by simple calcination. ZIF-8 calcination is considered an easy route to obtain porous ZnO with high photocatalytic performance.[26,27] The porous structure with abundant active sites can not only facilitate the absorption of more organic pollutants, but also solve the problem of volume recombination by increasing photon absorption and charge carrier transfer.[9,28] Therefore, porous MOF-derived metal oxide heterojunction have an important role in wastewater treatment.

In this study, a series of mesoporous α-Fe$_2$O$_3$/ZnO heterojunction composites were fabricated using α-Fe$_2$O$_3$/ZIF-8 as sacrificial template by simple calcination in air atmosphere. The effect of pore modification on MB degradation is also discussed. Reusability and trapping experiments of MOF and MOF-derived metal oxide composites were evaluated to compare their activities. Finally, we also investigate in detail the possible mechanism of mesoporous α-Fe$_2$O$_3$/ZnO heterojunction composites.

Experimental

Material

Zinc(II)nitrate tetrahydrate (Zn(NO$_3$)$_2$·4H$_2$O) (Merck, 99%), 2-methylimidazole (Merck, 99%), glacial acetic acid (Merck, 99%), methanol (Merck, 99.9%), iron(III)oxide (α-Fe$_2$O$_3$) (Merck, 99%), triethylamine (TEA, Merck, 99%), isopropyl alcohol (Sigma-Aldrich), dimethyl sulfoxide (Merck), ascorbic acid (Merck), demineralized water, and methylene blue (Merck).

Synthesis of ZIF-8 and porous ZnO

The ZIF-8 was synthesized in the media of 2% acetic acid solution.[29] The process of synthesis was carried out by dissolving 1.7848 g of Zn(NO$_3$)$_2$·4H$_2$O in 10 mL of 2% acetic acid, and dissolving 4.4916 g of 2-methylimidazole in a solvent mixture of 15 mL of demineralized water and 7.8 mL of TEA. The two solutions were then mixed until a white precipitate formed and allowed to stand at room temperature for 24 hours. Then the precipitate was separated by centrifugation, washed successively with demineralized water and methanol, dried at 60 °C for 12 hours and labelled as ZIF-8. A certain amount of ZIF-8 was placed in the crucible boat and calcined in an air atmosphere at 600 °C for 2 hours. The collected powder was labelled as ZnO.

Synthesis of α-Fe$_2$O$_3$/ZIF-8 and porous α-Fe$_2$O$_3$/ZnO

The α-Fe$_2$O$_3$/ZIF-8 composites were synthesized using the same procedure as for ZIF-8 synthesis, with addition of α-Fe$_2$O$_3$ at 10, 25 and 50% to the weight of ZIF-8, to the solution of Zn(NO$_3$)$_2$·4H$_2$O in 2% acetic acid (Fig. 1). The composites were then labelled as Fe(10)ZIF-8, Fe(25)ZIF-8 and Fe(50)ZIF-8, respectively. Further, after calcination, the obtained powders were labelled as Fe(10)ZnO, Fe(25)ZnO and Fe(50)ZnO, respectively.

Material characterizations

Powder X-ray diffraction patterns to obtain the crystal phase were obtained using the Xpert MPD diffractometer with Cu Kα irradiation source at a range of 5 to 100° ($\lambda = 1.5406$ \, 40 kV, 30 mA). To know the characteristic functional group of the synthesized materials using the Shimadzu 8400S infrared spectrophotometer at wavenumbers in the range of 400–4000 cm^{-1}. Field emission scanning electron microscopy with energy dispersive X-ray spectroscopy (FESEM-EDX) characterization was performed to observe the micro and mesostructure morphology and distribution of element at the samples. The surface area and features of pore structure were calculated using the Quantachrome NovaWin Gas Sorption Analyzer based on the Barret–Joyner–Halender (BJH) and Brunauer–Emmett–Teller (BET) models, respectively. Thermogravimetric analyses (TGA) of the samples were recorded using the PerkinElmer Pyris 1 Analyzer (approximately ± 10 mg of the samples) to study the thermal stability of ZIF-8 synthesized. The samples were put into a holder before being heating rate of 10 °C min^{-1} and at temperatures in the range of 30–900 °C. UV-vis diffuse reflectance spectra (DRS) were measured using the Agilent Cary UV-vis spectrophotometer to study the optical absorption properties. Photoluminescence (PL) was acquired using the fluorescence spectrometer Shimadzu RF-5310. The excitation wavelength of 320 nm was used to further obtain the optical properties of the materials. The EIS plots were performed by a CHI660E instrument. Electrochemical station with Ag/AgCl, Pt and 0.5 M Na$_2$SO$_4$ as reference electrode, counter electrode and electrolyte solution with full-spectrum of illumination. In photoelectric experiments, a typical materials were dropped cast on FTO at −0.2 V vs. saturated calomel electrode (SCE) at
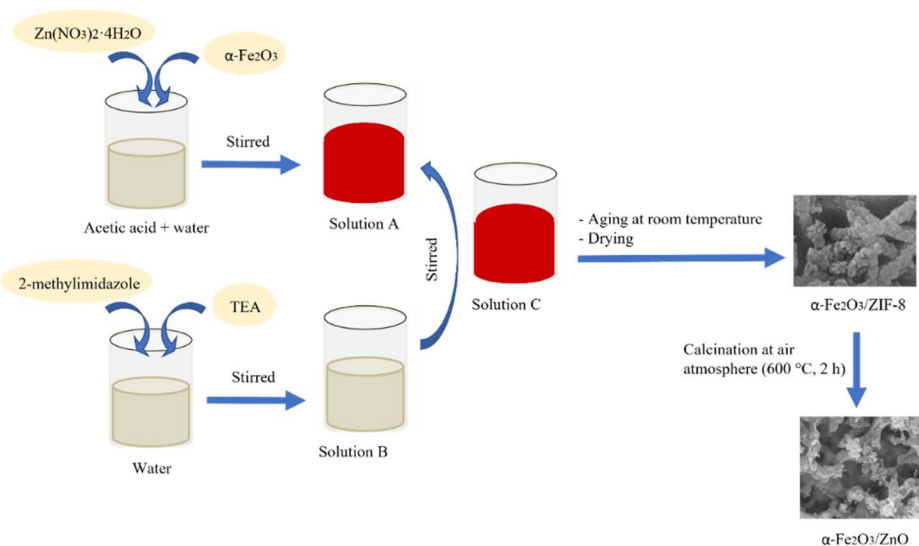
Fig. 1 The proposed schematic illustration of the mesoporous α-Fe₂O₃/ZIF-8 heterojunction.

a frequency of 0.1 to 10^5 Hz. Mott Schottky plots were measured under the ambient condition at a frequency of 0.5 kHz and an amplitude of 0.01 V. The concentration of MB after each reaction were recorded using the Thermo Scientific GENESIS 10S UV-vis spectrophotometer at a wavelength of 663 nm.

Adsorption and photocatalytic performances

The adsorption experiment of the synthesized material on MB in water was performed in a batch system with an initial concentration of MB 30 mg L^{-1} and an adsorbent dose of 5–30 mg in 30 mL for 120 minutes. The adsorption process at various contact times was also conducted to obtain the equilibrium adsorption time. The equilibrium adsorption time was used as the duration of the dark condition in the photocatalytic process. The concentration of MB in the remaining solution was measured using the UV-vis spectrophotometer at a wavelength of 663 nm.

The photocatalytic process was investigated by MB degradation under UV LED lamp (Fig. 2). A 12 W UV-LED lamp with

a 365 nm cut-off was used as the light source. The irradiation distance between the lamp and the sample was 15 cm. Before the photocatalytic tests, all the photocatalysts were activated at 60 °C for 24 hours. In brief, 30 mg of photocatalyst was mixed with 30 mL of 30 mg L^{-1} MB solution in batch system. The temperature of the photocatalytic process was maintained at 30 °C, and stirred for 60 and 40 min, for α-Fe₂O₃/ZIF-8 and α-Fe₂O₃/ZnO composites respectively, in the dark condition to achieve the adsorption–desorption equilibrium. After reach the equilibrium, the sample was irradiated with time intervals of 30, 60, 90, 120 and 150 minutes. The concentration of MB remained after photocatalytic process was analyzed using a UV-vis spectrophotometer. In this experiment, the photocatalyst dose, irradiation time and MB concentration were varied to test the effectiveness of the photocatalyst. Photocatalytic kinetic of the synthesized material was evaluated by zero order (eqn (1)), first order (eqn (2)) and second order (eqn (3)) as follows to study the behavior of decomposed dye solution:

$$C_0 - C_t = K_0 t \quad (1)$$

$$\ln(C_0/C_t) = K_1 t \quad (2)$$

$$\frac{1}{[C_0]} - \frac{1}{[C_t]} = K_2 t \quad (3)$$

where K_0, K_1 and K_2 are the rate constant of the zero, first and second order reaction, respectively. C_0 (mg L^{-1}) and C_t (mg L^{-1}) are the MB concentration at initial and any time t (min), respectively.

Radical trapping experiments

The detection of active species was performed by trapping experiments using different scavengers. The method of trapping experiment is the same as a photocatalytic reaction with the addition of different corresponding scavengers. In these research, we used scavengers IPA (scavenger for ˙OH), DMSO
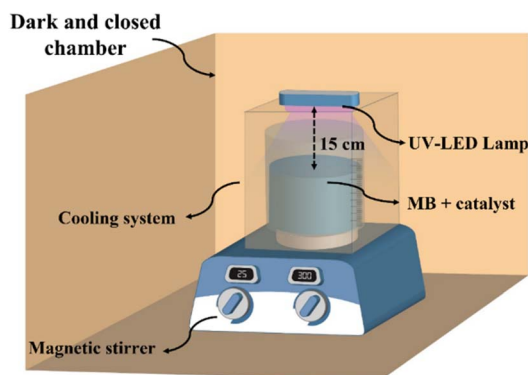

Fig. 2 Schematic illustration of the experimental setup of photocatalytic activity.

(scavenger for electron), methanol (scavenger for hole), and ascorbic acid (scavenger for $\cdot O_2^-$). In each experiment, 30 mg of photocatalyst was added to 30 mg L^{-1} MB solution, and the mixture was stirred in the dark for 60 minutes (for Fe(25)ZIF-8) and 40 minutes (for Fe(25)ZnO) to achieve adsorption–desorption equilibrium before being exposed to a UV-LED lamp for 150 minutes.

Results and discussion

Material characterizations

XRD characterization was conducted to determine the crystallinity and phase structures of the synthesized materials. The XRD pattern of ZIF-8 is shown in Fig. 3a in which the characteristic peaks are exhibited at $2\theta = 7.29, 10.39, 12.69, 16.38$ and $17.96°$. These peaks were consistent with previous research,[29]

which proves that ZIF-8 with high purity was successfully synthesized. A commercial α-Fe_2O_3 has characteristic peaks in the region of $2\theta = 24, 32.97, 35.46, 40.69$ and $53.89°$, correlating to the planes (0 1 2), (1 0 4), (1 1 0), (1 1 3) and (1 1 6), respectively, according to JCPDS 33-0664. All off the diffraction peaks in Fe(10)ZIF-8, Fe(25)ZIF-8 and Fe(50)ZIF-8 show the same main diffraction peaks of ZIF-8 and α-Fe_2O_3 with slight reduction in their intensities. Furthermore, other peak impurities were not detected in a series of MOF composites which prove the high purity of the MOF composites (Fig. 3a). Based on Table 1 it is shown that the main peaks of series MOF composites are produced a minor shifting towards the lower diffraction angles compared to the pristine ZIF-8 without any significant shifting and still maintain the crystal lattice structure.[30] After calcination at 600 °C, all materials showed to ZnO structure (Fig. 3b). It can be inferred that there is no peak of impurity detected in all
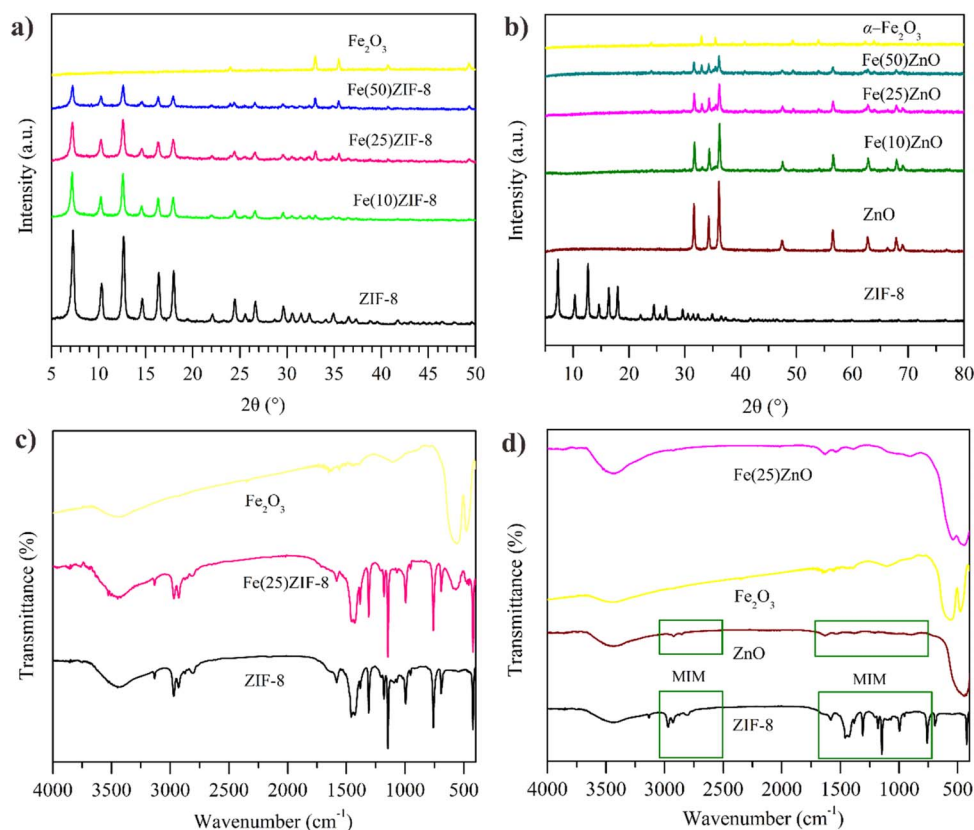

Fig. 3 XRD pattern of (a) MOF composites (b) MOF-derived metal oxide and FTIR spectra of (c) MOF composites (d) MOF-derived metal oxide.

Table 1 Quantitative analysis of MOF composites

| Sample | 2θ (°) | | | | | Crystallinity (%) |
	Peak 1	Peak 2	Peak 3	Peak 4	Peak 5	
ZIF-8	7.36 (2081.01)	10.42 (854.42)	12.69 (2431.88)	16.40 (1218.81)	18.07 (1287.07)	100
Fe(10)ZIF-8	7.19 (1376.11)	10.27 (513.64)	12.60 (1295.09)	16.30 (572.71)	17.95 (600.69)	55.35
Fe(25)ZIF-8	7.27 (1019.58)	10.28 (532.32)	12.59 (1180.60)	16.35 (467.75)	17.89 (543.19)	47.54
Fe(50)ZIF-8	7.27 (635.80)	10.27 (280.65)	12.61 (640.18)	16.35 (278.12)	17.90 (315.41)	27.30

Table 2 Quantitative analysis of metal oxide derived MOF

Material	2θ			Crystallinity (%)
	Peak 1	Peak 2	Peak 3	
ZnO	31.63 (2213.12)	34.29 (1558.93)	36.11 (3270.94)	100
Fe(10)ZnO	31.73 (1394.12)	34.35 (988.48)	36.21 (2279.69)	59.21
Fe(25)ZnO	31.68 (851.96)	34.32 (644.46)	36.14 (1334.90)	35.96
Fe(50)ZnO	31.59 (514.21)	34.26 (396.10)	36.16 (742.79)	20.98

MOF-derived metal oxide composites, and a peak have a unique crystal face and accordance with ZnO in the region of $2\theta =$ 31.63, 34.29 and 36.11° correlating to the plane of (1 0 0), (0 0 2), and (1 0 1). It can be observed that the diffractogram of Fe(10) ZnO, Fe(25)ZnO and Fe(50)ZnO have characteristic peaks both ZnO and α-Fe$_2$O$_3$. The characteristic peak of ZnO does changeless, indicating that α-Fe$_2$O$_3$ is only on the surface of ZnO through physical action. These results indicate the successful preparation of MOF-derived metal oxide composites has been confirmed.

Based on Tables 1 and 2, after the addition of α-Fe$_2$O$_3$, the intensity of all composite decreased significantly. Table 1 shows the correlation between intensity and crystallinity values in MOF composites and Table 2 for MOF-derived metal oxide composites.

Low crystallinity can also be indicated by the presence of broader diffraction peaks.[30,31] The broader peaks are due to the presence of α-Fe$_2$O$_3$ which have an amorphous structure that has been successfully loaded on ZIF-8 via in situ method with the assumption that in situ nucleation and growth of ZIF-8 on α-Fe$_2$O$_3$ favor decreasing the scattering of light hitting an aligned surface.[32]

The FTIR spectra of ZIF-8 shows the stretching vibration of –OH at 3448 cm^{-1}. The adsorption peak located at 3132 cm^{-1} correspond to C–H stretching vibration from methyl group in imidazole ring. The wavenumbers located at 2970 and 2928 cm^{-1} were related to the presence of C–CH$_3$ from acetic group and the stretching of aliphatic C–H methyl group from aromatic linker.

At lower wavenumbers at 1178 cm^{-1} and 995 cm^{-1} correspond to the in-plane and out-of-plane bending from the ligand imidazole. The lower peak around at 1581 cm^{-1} attributed to stretch mode of C=N. The absence of peak located at 1849 cm^{-1} from the bending and stretching vibration of N–H indicates that the 2-methylimidazole has been successfully deprotonated with the presence of TEA. Zn–N stretching mode in the wavenumber 422 cm^{-1}.[29] The spectra of α-Fe$_2$O$_3$ as displayed in Fig. 3c the wavenumber at 3435 cm^{-1} is attributed to asymmetrical stretching vibration and molecular deformation of the water adsorbed. The peak at 559.27 and 476.47 cm^{-1} is due to the Fe–O stretching vibration.[33] The Fe(25)ZIF-8 (Fig. 3c) possess characteristic absorption bands of both ZIF-8 and α-Fe$_2$O$_3$. These result signified that there were no impurities found in Fe(25)ZIF-8.

The spectra of ZnO indicated the wavenumber at 426 cm^{-1} can be attributed of stretching Zn–O band. Same as spectra

FTIR of α-Fe$_2$O$_3$, the presence wavenumber at 3446 cm^{-1} is attributed to asymmetrical stretching vibration and molecular deformation of the water adsorbed.[34] The spectra of Fe(25)ZnO (Fig. 3d) showed combination peaks of ZnO and α-Fe$_2$O$_3$ and did not show other peaks. These results indicate that calcination at 600 °C can remove organic components from the ligand and produce ZnO.

The morphology of ZIF-8 based on Fig. 4a is spherical morphology. Furthermore, the morphology of ZnO (Fig. 4b) retains the morphology of ZIF-8 with the lower agglomeration. FESEM image of Fe(25)ZIF-8 and Fe(25)ZnO are displayed in Fig. 4c and d. Fe(25)ZIF-8 is formed by particles of nearly spherical morphology with agglomeration and resembling a starfish. While Fe(25)ZnO, whether they are nearly spheric or not and the dense network can not be observed. In this case, it is obvious from a closer look at the magnified in Fig. 4d where their morphology was maintained spheric with lower agglomeration than Fe(25)ZIF-8. The resulting agglomeration is a consequence of the high surface energy and van der Waals forces. Greater interactions between nanoparticles and higher tensile forces occur due to the high surface area. These results are linier with the N$_2$ physisorption which ZIF-8 and Fe(25)ZIF-8 have a higher surface area than ZnO and Fe(25)ZnO. Besides, higher attractive force between nanoparticles causes the presence of strong adhesion, resulting in agglomeration.[35] The particle size histograms estimated the size distribution (Fig. 4e– h) of ZIF-8, ZnO, Fe(25)ZIF-8 and Fe(25)ZnO at 38.83, 36.84, 45.17 and 39.35 nm, respectively. The EDX mapping of ZIF-8, ZnO, Fe(25)ZIF-8 and Fe(25)ZnO are shown in Fig. 4i–l and Table 3 also reveal elemental composition and distribution in this samples. ZIF-8 consist of a homogeneous elemental distribution of zinc (Zn), nitrogen (N) and carbon (C) elements. The distribution uniform of zinc (Zn), nitrogen (N), carbon (C), iron (Fe) and oxygen (O) in the Fe(25)ZIF-8 reflects the successful synthesis using in situ method. The zinc (Zn) and oxygen (O) elements are uniformly distributed in ZnO. Fe(25) ZnO mapping demonstrated the homogeneous elemental distribution of zinc (Zn), iron (Fe) and oxygen (O) elements. The heat treatment causes a phase transformation which is proven by the loss of carbon and nitrogen elements from their frameworks. EDX mapping in line with diffractogram of XRD that there are no impurity detection and FTIR spectra that imidazolate ligand have been successfully removal after the heat treatment. Furthermore, from elemental mapping of Fe(25)ZIF-8 and Fe(25)ZnO, it can be known that Fe elements are equal distributed in the Fe(25)ZIF-8 and Fe(25)ZnO.
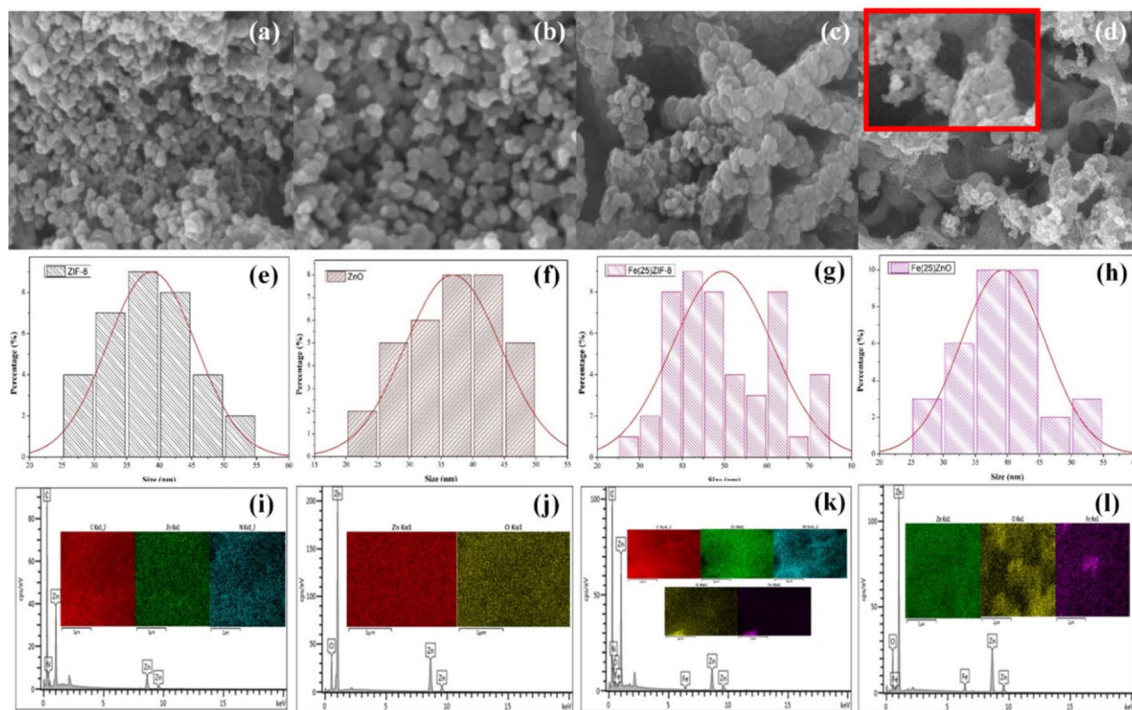
Fig. 4 FESEM image of (a) ZIF–8 (b) ZnO (c) Fe(25)ZIF–8 (d) Fe(25)ZnO, particle size distribution of (e) ZIF–8 (f) ZnO (g) Fe(25)ZIF–8 (h) Fe(25)ZnO, elemental mapping of (i) ZIF–8 (j) ZnO (k) Fe(25)ZIF–8 (l) Fe(25)ZnO.

The surface and porous properties of materials have an imperative impact on adsorption-photocatalytic performance. The surface area and feature of pore structure of materials were measured using BET characterization method based on N_2 physisorption. According to the IUPAC classification, ZIF-8 showed type I isotherms with micropore structure which is characterized by the amount of adsorbed increases sharply at the low pressure (Fig. 5a). The pristine ZIF-8 shows higher specific surface area and porosity than previous report (Table 4).[29] Based on Fig. 5a, Fe(10)ZIF-8 and Fe(25)ZIF-8 also classified as type I isotherms but their specific surface area and porosity are lower than pristine ZIF-8 (Table 3). Decreasing in

specific surface area and porosity may be due to the addition of α-Fe_2O_3.

After calcination, ZnO, Fe(10)ZnO and Fe(25)ZnO showed type-IV isotherms with the obvious hysteresis loop H3 at a relatively high pressure, due to the presence of adjacent small particles to produce a new larger cavity that was detected as slit-like pores (Fig. 5c).[36,37] The specific surface area and porosity of the ZnO, Fe(10)ZnO and Fe(25)ZnO can be seen in Table 4. The template method proves for production mesoporous metal oxide (ZnO and α-Fe_2O_3/ZnO) with high surface area than conventional synthesized ZnO (Table 5).[38–43] These results indicate that using ZIF-8 as a template with a high surface area could produce ZnO with a higher surface area than the synthesis of ZnO using a Zn precursor which has a low surface area. The change in isotherm type from type I to type IV indicates collapsing of the micropores in the ZIF-8 framework to mesopores due to the decomposition of organic ligands during the calcination produced heat energy that spreads over the entire surface and lead to the appearance of new lower surface area.[44] Although there was a change in the type of isotherm in MOF-derived metal oxide, the mesopore did not change significantly (Table 4) which was confirmed by FESEM of ZnO and Fe(25)ZnO (Fig. 4a and b) which still maintain a spheric morphology from their pristine. This shows that the use of MOF as a metal oxide template through calcination is an effective way to produce mesoporous metal oxide.

TGA characterization was performed to obtain the thermal stability of the synthesized materials (ZIF-8 and Fe(25)ZIF-8 composite) and to select the calcination temperature to produce metal oxide. According to Fig. 6, the thermogram of

Table 3 Elemental analysis using EDX

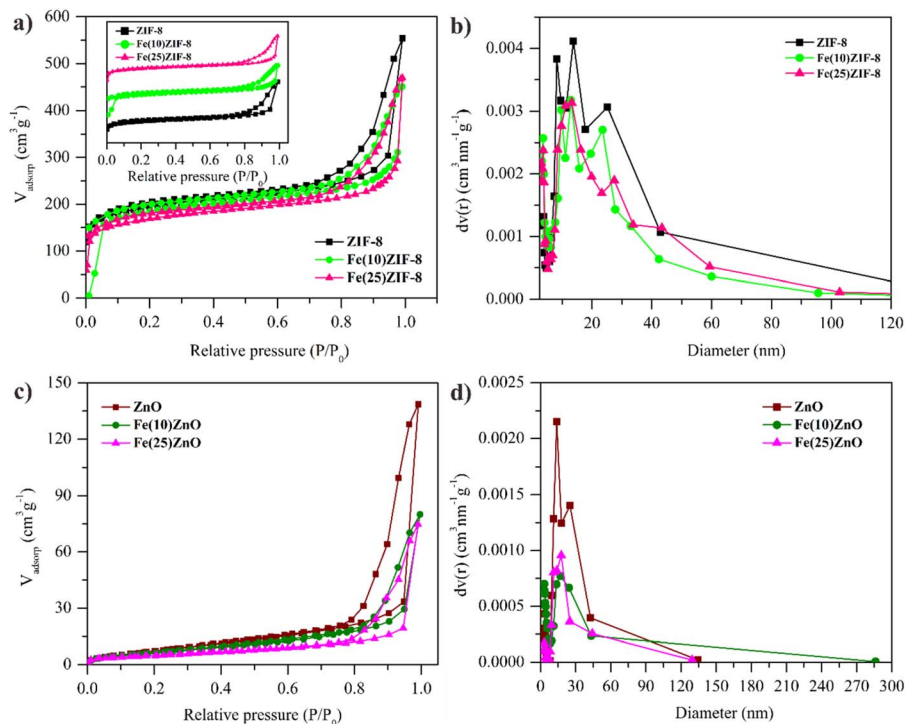| Material	Element	Content (%)
ZIF-8	Zn	11.8
	N	18.4
	C	69.8
Fe(25)ZIF-8	Zn	13.5
	N	16.4
	C	63.1
	O	6.5
ZnO	Fe	0.6
	Zn	77.5
	O	22.5
Fe(25)ZnO	Fe	76.3
	Zn	4.1
	O	19.6

Fig. 5 N_2 adsorption–desorption isotherm of (a) MOF composites (c) MOF-derived metal oxide and BJH pore distribution of (b) MOF composites (d) MOF-derived metal oxide.

Table 4 Physical properties of material

Material	S_{BET} (m^2 g^{-1})	V_p meso (cm^3 g^{-1})	V_p micro (cm^3 g^{-1})	V average (cm^3 g^{-1})	D meso (nm)	D_p average (nm)
ZIF-8	705.3	0.58	0.29	0.856	13.742	4.858
Fe(10)ZIF-8	665.9	0.42	0.28	0.726	12.93	4.19
Fe(25)ZIF-8	608.2	0.48	0.25	0.697	13.202	4.78
ZnO	32.63	0.22	0.01	0.214	13.814	26.28
Fe(10)ZnO	26.92	0.12	0.008	0.123	17.006	18.39
Fe(25)ZnO	17.99	0.11	0.006	0.115	17.678	25.7
ZIF-8[29]	538	0.166	0.2696	0.4356	—	3.24
ZnO (ZIF-8)[9]	16.9	—	—	0.088	—	—
ZnO (RP)[9]	0.56	—	—	0.00096	—	—

ZIF-8 underwent a weight decrease of 20.1% at temperature range of 25–330 °C. The weight loss of 20.1% indicated that evaporation of the adsorbed water molecules, the reactants did not react and were trapped within the framework of ZIF-8. The second weight reduction of 58.1% occurred in the range of 380–560 °C, which signalled that a thermal decomposition occurred on the framework of ZIF-8.[45] The ZIF-8 thermogram showed the thermal stability up to 380 °C.

Table 5 Comparison of the photocatalytic performance of ZnO in various synthesis method

| Material	Method	S_{BET} (m^2 g^{-1})	V_{pore} (cm^{-3} g^{-1})	Pollutant	Degradation efficiency (%)	Condition	Ref.
ZnO	Refluks	9.0687	0.037	Methylene blue	97.16	5 mg L^{-1}; 10 mL; 0.04 gram; 6 h	38
ZnO	Sol–gel	11.7	0.025	Methylene blue	74	10^{-5} M; 100 mL; 0.1 gram; 120 min	39
ZnO	Hydrothermal	12.07	0.027	Methylene blue	70	20 mg L^{-1}; 0.03 g; 150 mL; 120 min	40
ZnO	Hydrothermal	—	—	Methylene blue	60	20 mg L^{-1}; 50 mg; 25 mL; 60 min	41
ZnO	Hydrothermal	9.65	0.016	Methylene blue	85	5 mg L^{-1}; 30 mg; 100 mL; 210 min	42
ZnO	Hydrothermal	—	—	Methylene blue	71.7	5 mg L; 30 mg; 150 min	35
ZnO	Template	32.63	0.214	Methylene blue	98.7	30 mg L^{-1}; 30 mg; 150 min	This work
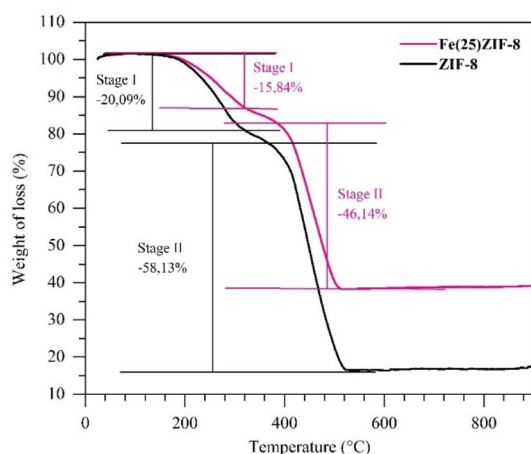
Fig. 6 TGA curve of ZIF-8 and Fe(25)ZIF-8.

The temperature increase of above 380 °C induced the formation of α-Fe$_2$O$_3$/ZnO. However, at a temperature range of 380–525 °C, organic components were still detected on the framework of Fe(25)ZIF-8. Pure α-Fe$_2$O$_3$/ZnO was formed at temperatures of above 525 °C. The TGA results showed that the loading of α-Fe$_2$O$_3$ can increase the thermal stability of the composite.[46] Fe(25)ZIF-8 has about 25% more weight than ZIF-8 which is derived from α-Fe$_2$O$_3$. The calculation to determine the amount of ZnO and Fe(25)ZnO produced using the ZIF-8 and Fe(25)ZIF-8 templates through the weight at 560 °C divided by the weight at around 400 °C.[47] Yield of ZnO and Fe(25)ZnO in this study are 21 and 45%, respectively. It can be known that the addition of α-Fe$_2$O$_3$ to obtain Fe(25)ZnO composite has been successfully carried out. Thus, based on the thermogram, the selected calcination temperature to produce ZnO and Fe(25)ZnO from ZIF-8 and Fe(25)ZIF-8 was 600 °C.

Optical properties

UV-Vis DRS were performed to calculate the wavelength of absorption and band gap (E_g) value of photocatalyst. The wavelength of the absorption is determined by extrapolating the part of the spectra on the horizontal side and rising sharply from the spectra defined as the intersection of the wavelengths and help to determine the E_g value. There are two absorption peaks in heterojunction composites around of 370 and 560 nm, which can be known to the attribute of the electronic transition from the VB to the CB due to the absorption of photon, O^{2-} → Zn^{2+} and O^{2-} → Fe^{3+} charge transfer processes, respectively.[1,3,48] UV-vis wavelength range of α-Fe$_2$O$_3$/ZnO is broader than the pristine semiconductor (ZnO and α-Fe$_2$O$_3$) which is correlated with the fabrication of the n–n heterojunction system by combining two semiconductors (ZnO and α-Fe$_2$O$_3$).[49,50] The E_g value of photocatalyst (Fig. 7b) was further calculated using Kubelka–Munk equation. The E_g values of pristine ZIF-8, ZnO and α-Fe$_2$O$_3$ are 3.17, 3.22 and 2.02, respectively. Besides, the E_g values of Fe(10)ZnO, Fe(25)ZnO and Fe(50)ZnO are 1.98, 1.95
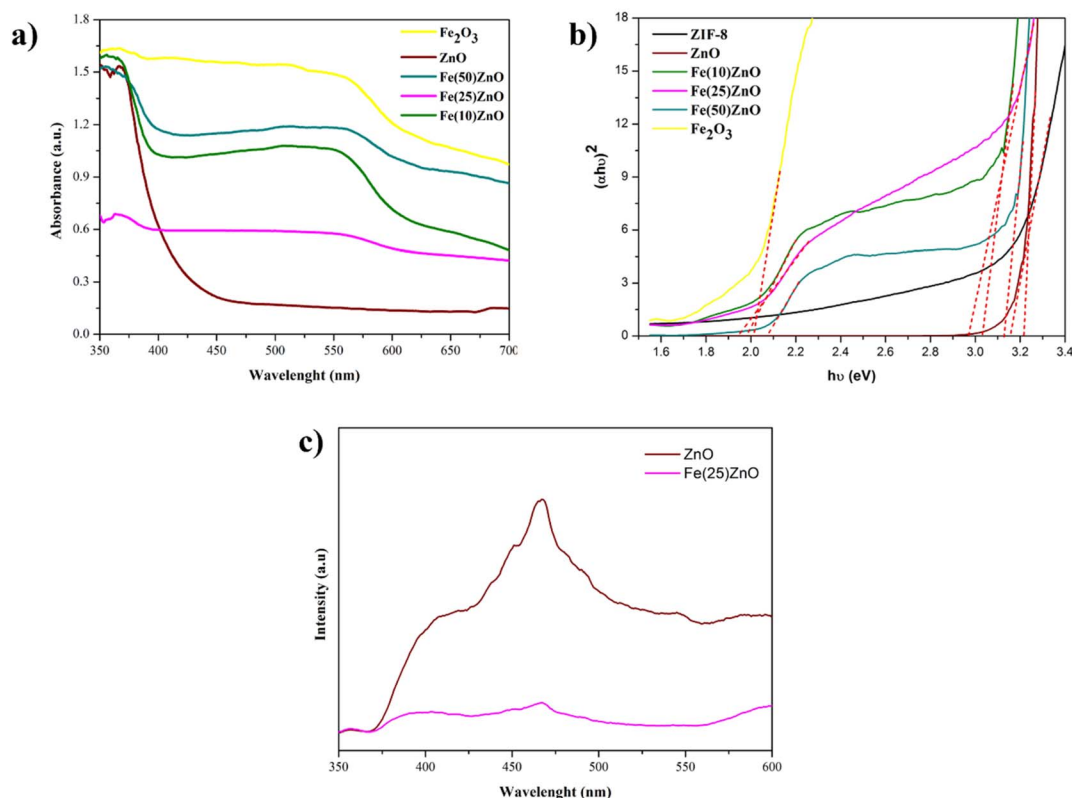

Fig. 7 (a) UV-vis DRS spectra (b) plot of $(\alpha h\nu)^2$ versus energy ($h\nu$) (c) PL spectra of ZnO and Fe(25)ZnO.

and 2.09 eV (E_{g1}) for the lower energy area and 3.1, 2.98 and 3.15 eV (E_{g2}) for the higher energy area. Based on the calculation, confirm a decreasing of E_g values in α-Fe$_2$O$_3$/ZnO due to the presence of redshift and extend the optical absorption properties to the visible range. The decreasing of E_g value results a lower energy required for excitation of electron from VB to CB thereby increasing the photocatalytic performance. The E_g value of ZnO generated using template method is not much different from the E_g value of ZnO generated by other methods.[8,40,51] Meanwhile, Fe(50)ZnO showed an increasing E_g value when compared to the other photocatalysts. This condition indicates that the optimum addition of α-Fe$_2$O$_3$ is 25%.[36] The addition of α-Fe$_2$O$_3$ greater than 25% causes the presence of agglomeration on the surface photocatalyst and covers the active site so the adsorption and photocatalytic processes will be decreased.[52]

Photoluminescence (PL) characterization is another important technique to reveal the separation efficiency of charge carriers in semiconductor materials. As presented in Fig. 7c, ZnO and Fe(25)ZnO show a similar feature of PL spectra, with the peak centered at 468 nm. The PL intensity of Fe(25)ZnO is significantly lower compared to the pristine ZnO, which is attributed to the suppression of charge carriers recombination in Fe(25)ZnO. The presence of n–n heterojunction system between ZnO and α-Fe$_2$O$_3$ may be responsible for this suppression of carriers' recombination due to the more improve effectiveness separation of electron–hole pairs as previously reported.[53]

In addition to PL analysis, we also performed Mott–Schottky measurement over ZnO and Fe(25)ZnO to verify the formation of n–n heterojunction in Fe(25)ZnO. As presented in Fig. 8, both ZnO and Fe(25)ZnO show positive slopes, which indicate the nature of n-type semiconductor with electrons as majority charge carriers.[54,55] Note that Fe(25)ZnO consists of α-Fe$_2$O$_3$ and

ZnO, in which α-Fe$_2$O$_3$ is an n-type semiconductor.[54,55] Moreover, the carrier densities of ZnO and Fe(25)ZnO can be calculated according to eqn (4):

$$C_{sc}^{-2} = \pm \frac{2}{q\varepsilon\varepsilon_0 N_d}\left(V - V_{FB} - \frac{KT}{q}\right) \qquad (4)$$

where q is the electronic charge, N_d is the carrier density, ε is the dielectric constant of the semiconductor ($\varepsilon = 10$ for ZnO), ε_0 the permittivity of free space, C is the capacitance that can be obtained from the Mott–Schottky plot and the value of V, V_{FB}, q, K and T can be obtained from the Mott–Schottky slope of the Mott–Schottky plot.[54] The calculated carrier densities (N_d) for ZnO and Fe(25)ZnO are 3.6×10^{19} and 6.3×10^{19} cm^3, respectively. Clearly, Fe(25)ZnO has a higher carrier density than ZnO, which may be attributed to the presence of n–n heterojunction. Therefore, the PL analysis and the Mott–Schottky analysis collectively verify the formation of n–n type heterojunction between α-Fe$_2$O$_3$ and ZnO in Fe(25)ZnO as evidenced by the retained n-type nature of the materials, higher charge carriers density, and the suppressed charge carriers' recombination.

Photocatalytic activity

Evaluation of photocatalytic performance. To evaluate the adsorption and photocatalytic performance of MOF and MOF-derived metal oxide composites, MB was selected as a pollutant model for photocatalytic degradation under UV LED lamp as shown in Fig. 8c. Before the photocatalytic test, the adsorption–desorption equilibrium in the dark condition was achieved after 60 min for MOF composites and 40 min for MOF-derived metal oxide composites. As presented in Fig. 9a and b, the MOF composites have better performance in the dark conditions than MOF-derived metal oxide composites against MB removal. This could have been due to the high surface area from MOF composites which support a higher capacity
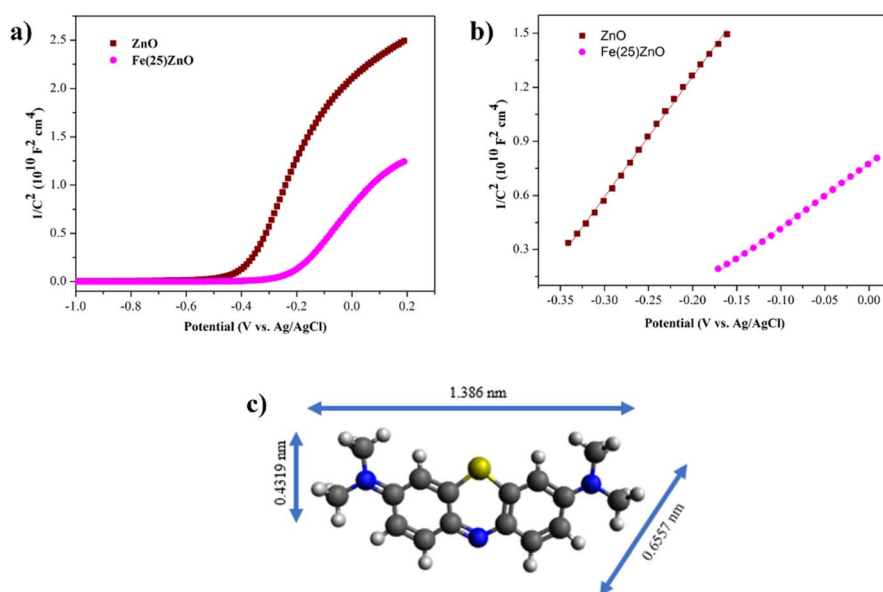

Fig. 8 (a) Mott–Schottky plots (b) linear fit plots of Mott-Schottky for ZnO and Fe(25)ZnO (c) structure of methylene blue.
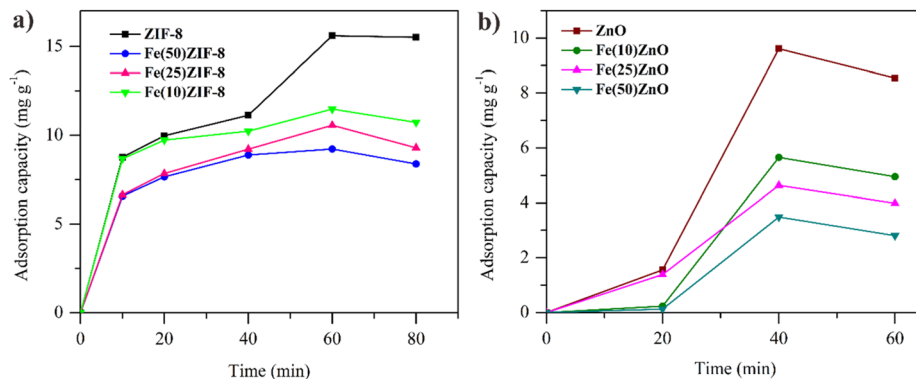
Fig. 9 Adsorption capacity in methylene blue solution ($W = 30$ mg, $C_0 = 30$ mg L^{-1}, $V = 30$ mL) of (a) MOF composites (b) MOF-derived metal oxide.

adsorption than MOF-derived metal oxide composites.[56] The higher adsorption capacity in MOF composites might occur due to the coordination bonding, hydrogen bonding and π–π stacking interactions of MOF composites with MB surface.[57] Coordination effect occurs between the donor electron in N from MB and the acceptor electron in the unoccupied Zn orbital in all material. The π–π stacking interaction present between the benzene ring in MB and the imidazole ring.[58,59]

However, the difference in adsorption capacity between ZIF-8 and ZnO did not show the significant result due to the ZnO has a nearly same mesopore with ZIF-8. Calzada *et al.*, reported that the adsorption capacity of ZnO in MB removal of 7 mg g^{-1}

was lower than ZnO in this report due to the lower mesopore.[60] So that the use of MOF as a metal oxide template can be used as an effective method to improve the adsorption performance of metal oxides.

During the 150 min irradiation the degradation of MB was negligible without the presence of photocatalyst indicating the stability of MB in water under UV LED irradiation. At the same time, there was a significant increase in the MOF-derived metal oxide composites with better performance than pristine ZnO and α-Fe₂O₃ due to presence of n–n heterojunction (Fig. 11a).

The appearance of n–n heterojunction increased the ability of MOF-derived metal oxide composites to degrade MB through
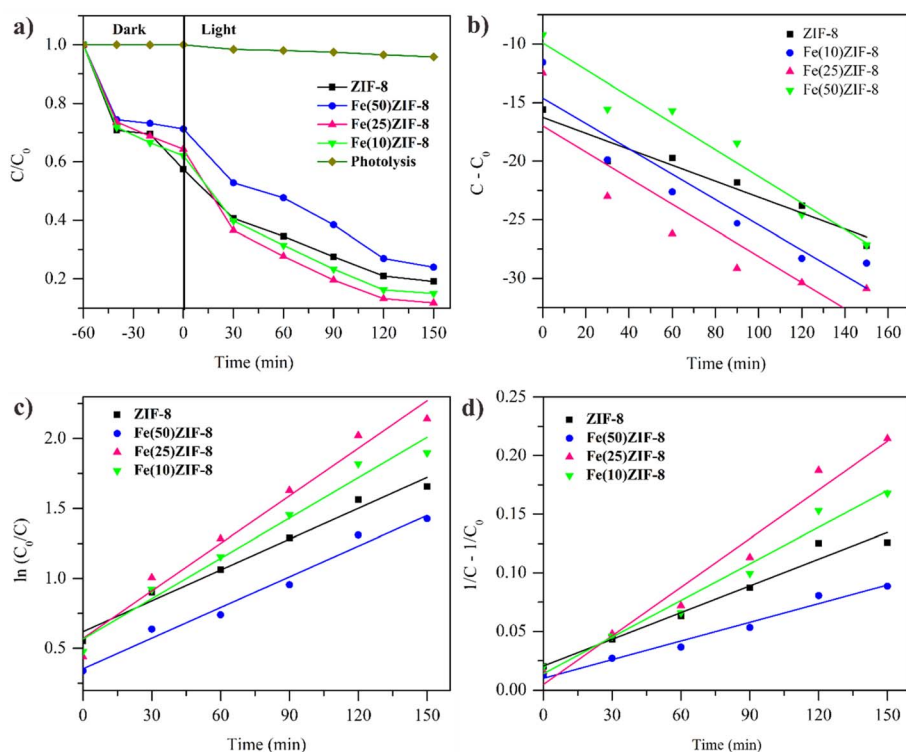

Fig. 10 (a) Effect of irradiation light on the degradation of methylene blue of MOF composites ($W = 30$ mg, $C_0 = 30$ mg L^{-1}, $V = 30$ mL) and kinetic plot (b) zero order (c) first order (d) second order.
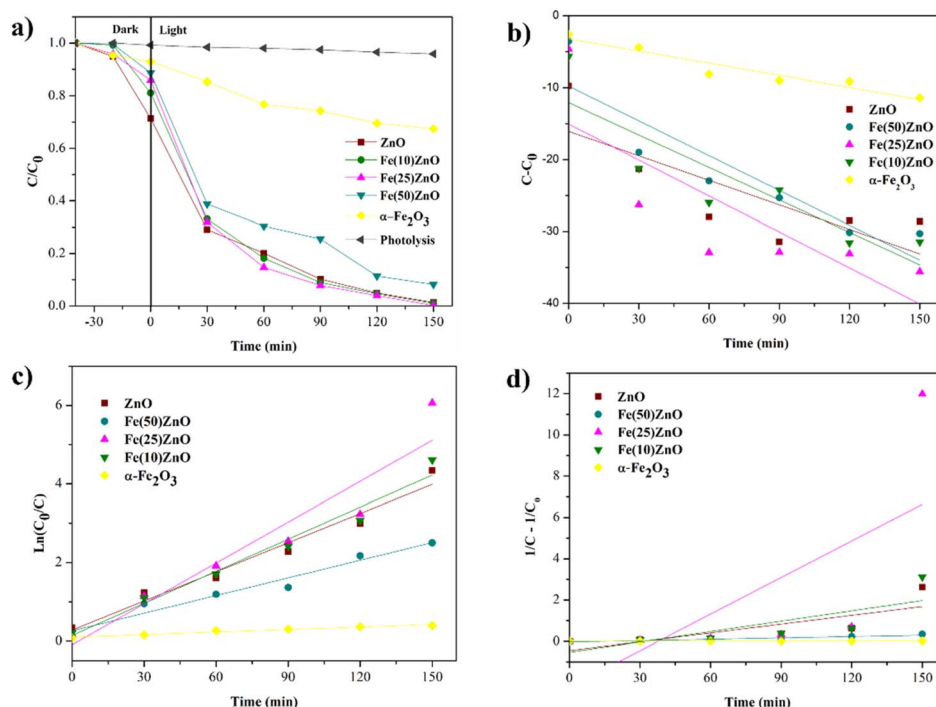
Fig. 11 (a) Effect of irradiation light on the degradation of methylene blue of MOF-derived metal oxide ($W = 30$ mg, $C_0 = 30$ mg L^{-1}, $V = 30$ mL) and kinetic plot (b) zero order (c) first order (d) second order.

broader photon absorption range, lower recombination rate of carriers, higher redox capability and presence of pores avoid the volume recombination.[9] These results prove that the combination of two semiconductors can overcome the shortcomings caused by one semiconductor. Photocatalytic performance can be increased with the addition of α-Fe$_2$O$_3$, but the excessive of α-Fe$_2$O$_3$ can decrease the photocatalytic performance. Fig. 10a and 11a show that the effect of adding 10 and 25% α-Fe$_2$O$_3$ in composites Fe(10)ZIF-8, Fe(25)ZIF-8, Fe(10)ZnO and Fe(25)ZnO has better photodegradation than that of ZIF-8 and ZnO. However, the addition of 50% α-Fe$_2$O$_3$ in composites Fe(50)ZIF-8 and Fe(50)ZnO has lower photodegradation than ZIF-8 and ZnO. Excessive of α-Fe$_2$O$_3$ can be closed the surface active sites and increased electron–hole recombination.[61,62]

In order to evaluate the kinetic behavior degradation of MB during photocatalytic process, experimental data of all photocatalyst were fitted into zero, first and second order and shown in Fig. 10b–d for MOF composites, Fig. 11b–d for MOF-derived metal oxide and Table 6 show the highest value of R^2 correlation coefficient was concluded that the photocatalytic process followed the first order kinetic (ln $C_0/C_t = kt$). The rate constant of the Fe(25)ZnO was 4.7 times larger than that of the ZIF-8. The higher degradation rate constant could be attributed to lower recombination of volume and charge carriers owing to synergistic effect mesoporous structure with n–n heterojunction.[44,63] Compared with other previously reported photocatalysts (Table 7), the Fe(25)ZnO behaved itself as a highly efficiency degradation for MB.

Table 6 The kinetic value of photocatalytic MB by various photocatalyst

Photocatalyst	Order 0		Order 1		Order 2	
	Rate constant (mol^{-1} Ls^{-1})	R_0^2	Rate constant (min^{-1})	R_1^2	Rate constant (L mg^{-1} min^{-1})	R_2^2
ZIF-8	0.0004	0.0003	0.0074	0.9815	0.0008	0.9716
Fe(10)ZIF-8	0.0204	0.0848	0.0096	0.9762	0.001	0.976
Fe(25)ZIF-8	0.0281	0.2639	0.0113	0.974	0.0014	0.9706
Fe(50)ZIF-8	0.0149	0.0182	0.0073	0.9799	0.0005	0.9771
ZnO	0.1137	0.6343	0.0247	0.9686	0.0142	0.6252
Fe(10)ZnO	0.1506	0.7801	0.0272	0.9731	0.0167	0.6111
Fe(25)ZnO	0.1668	0.6458	0.6458	0.9068	0.0591	0.4776
Fe(50)ZnO	0.1615	0.8276	0.015	0.9596	0.0021	0.8753
α-Fe$_2$O$_3$	0.0562	0.921	0.0021	0.9626	0.0001	0.9371

Table 7 Comparison of the photocatalytic performance of Fe(25)ZnO with other photocatalyst

Photocatalysts	Method	Pollutant	Efficiency degradation (%)	Time (min)	Condition	Ref.
SnO_2, α-Fe_2O_3/SnO_2	Hydrothermal	Methylene blue	40, 70	240	8 mL MB, 5 mg L^{-1}, 500 W Hg lamp	17
ZnO, α-Fe_2O_3/ZnO	Wet preparation. Chemical deposition	Methylene blue	59, 94.25	60	25 mL, 16 mg L^{-1}, 300 W Hg lamp	3
TiO_2, α-Fe_2O_3/TiO_2	Sol–gel	Methylene blue	30, 92	180	100 mL, 10 mg L^{-1}, 1 gram, 500 W Xe lamp	18
α-Fe_2O_3, mg/α-Fe_2O_3	Wet preparation	Methylene blue	5, 36	80	15 mL, 5 mg L^{-1}, 7.5 mg, 500 W Xe lamp	64
Cu_2O, α-Fe_2O_3/Cu_2O	Wet preparation, mechanochemical	Methylene blue	40.5, 81	45	10 mL, 2 mg L^{-1}, 0.4 g, 40 W tungsten lamp	65
Co doped ZnO	Hydrothermal	Methylene blue	96	120	10 mL, 10 mg L^{-1}, 40 W incandescent lamp	66
Co^{2+}-ZnO@SSM	Hydrothermal	Methylene blue	97.2	180	100 mL, 10 mg L^{-1}, 40 W incandescent lamp	67
Fe(25)ZnO	Template	Methylene blue	99.7	150	30 mL, 30 mg L^{-1}, 30 mg, LED 12W	This work

Effect of operational variables

Effect of photocatalyst dose. It is well known that dose of photocatalyst affects the adsorption-photocatalytic performance, which is one of the parameters that must be considered to support the success of the research. Thus, it is importance to determine and analyze its optimal dose of photocatalyst. The photocatalyst is mixed with 30 ppm MB at different doses. The effects of different doses on MB degradation is displayed in Fig. 12a and b. As observed from the diagram, the performance of all photocatalyst (MOF composites and MOF-derived metal oxide composites) increased with the increasing of the doses until the maximum dose was achieved at 30 mg. The highest efficiency degradation of 96.03% was observed at the 30 mg per 30 mL Fe(25) ZnO. When the dose is not optimal, the photocatalyst is not enough to absorb photon so the performance value is low. The use of an optimal dose causes the availability of an optimal surface active site to absorb photons resulting in a large number of charges and radicals to degrade MB.[68,69]

Effect of initial concentration. Based on Fig. 13 photocatalytic performance of ZnO, Fe(10)ZnO and Fe(25)ZnO (three catalyst

with higher photocatalytic performance) were decreased due to the increasing of MB concentration. When the MB concentration was 20 mg L^{-1}, all photocatalyst can degrade 100% of MB and Fe(25)ZnO can degrade 100% MB at 120 min. At lower concentration, the frequency of collisions between MB and photocatalyst was optimal due to the abundance of active site on photocatalyst, leading to the higher of the degradation. At higher concentration of MB, all photocatalyst showed decreasing performance, but Fe(25)ZnO still produced higher degradation performance up to 91.4%.

This is due to the unbalanced interaction between photons and surface of photocatalyst with the MB molecules. The increasing of MB will resist the direct interaction of photons with surface of photocatalyst and cause saturation thereby reducing the photon absorption. This situation causes photo generation to be hampered.[70]

Trapping experiment

Investigation on the active species that contributes to the MB degradation was carried out by means of a trapping experiment (Fig. 14). To study the role of active species, IPA (scavenger for
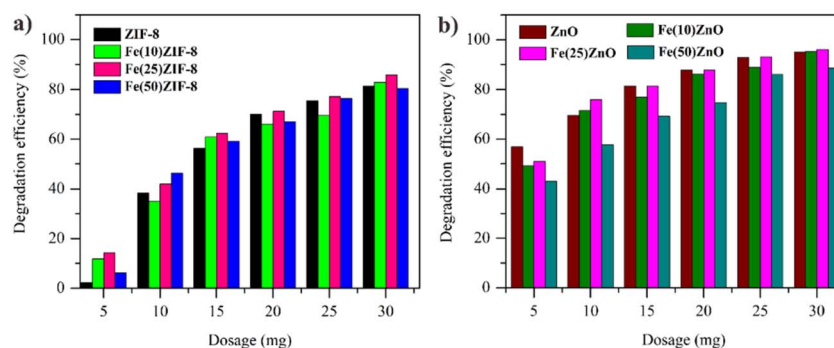

Fig. 12 Effect of dosage on degradation of MB (a) MOF composites (b) MOF-derived metal oxide (dosage = 5–35 mg, [MB] = 30 mg L^{-1}, t in dark = 60/40 min, t in uv light = 150 min).
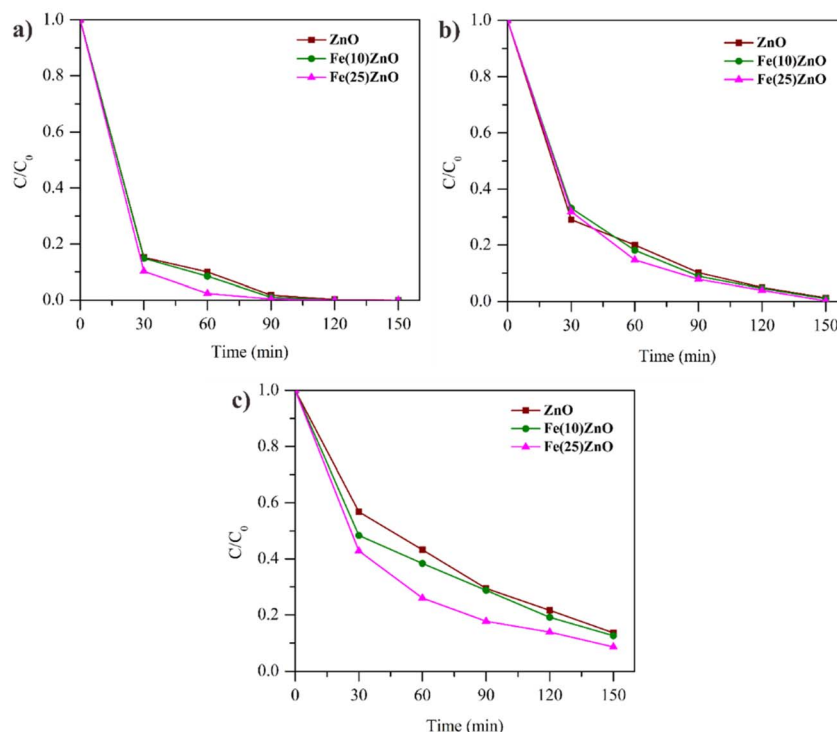
Fig. 13 Effect of MB concentration on the degradation efficiency (a) 20 mg L^{-1} (b) 30 mg L^{-1} (c) 40 mg L^{-1}.

$^{\bullet}OH$), DMSO (scavenger for electron), methanol (scavenger for hole) and ascorbic acid (scavenger for $^{\bullet}O_2^-$) were served as scavengers. The addition of trapping agent in Fe(25)ZIF-8 decreased the initial degradation performance of 88.25% to 73.78, 79, 81.4 and 74.10%, respectively (Fig. 14a).

The trapping experiment showed that electrons and $^{\bullet}O_2^-$ both had a significant contribution in degrading MB. This was proven with a more negative conduction band edge potential (E_{CB}) ZIF-8 value compared to the $O_2/^{\bullet}O_2^-$ potential of -0.33 eV, where both values had a difference of -1.2 eV. The low E_{CB} value of ZIF-8

made the reduction of O_2 to $^{\bullet}O_2^-$ easier. When DMSO was added with the purpose of capturing electrons, there was a decreasing in the number of electrons that were used to reduce O_2 to $^{\bullet}O_2^-$, thus diminishing the photocatalytic performance.

On the other hand, the addition of ascorbic acid caused the second largest reduction in the amount of electrons after DMSO, in which the number of electrons captures also affected the amount of $^{\bullet}O_2^-$ produced.[58,71] The results indicate that electrons and $^{\bullet}O_2^-$ is the leading free radicals species in MB degradation over Fe(25)ZIF-8.
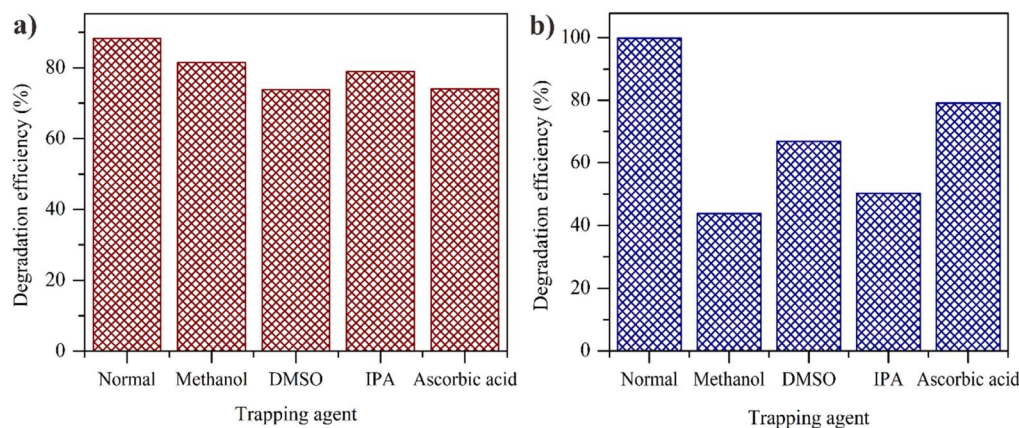

Fig. 14 Trapping experiments of active species in the photocatalytic reaction with 60 min in the dark and 150 min in the visible light irradiation (a) Fe(25)ZIF-8 (b) Fe(25)ZnO (dosage = 30 mg, [MB] = 30 mg L^{-1}, t in dark = 60 min for Fe(25)ZIF-8 and 40 min for Fe(25)ZnO, t in uv light = 150 min).

The addition of DMSO, IPA, methanol and ascorbic acid as a trapping agent in Fe(25)ZnO reduced the initial degradation of 99.76% to 66.75, 50.26, 43.82 and 79.07%, respectively (Fig. 14b). The trapping experiment showed that ˙OH and holes both had a significant contribution in degrading MB. This was proven with a more positive the valence band edge potential (E_{VB}) ZnO value compared to the H_2O/˙OH potential of 2.34 eV. The low E_{VB} ZnO value made the oxidation of H_2O to ˙OH easier. When IPA and methanol were added, the amount of ˙OH and holes to oxidize H_2O decreased thereby diminishing the photocatalytic performance.[72,73] The results indicate that ˙OH and holes is the leading free radicals species in MB degradation over Fe(25)ZnO.

Based on the radical trapping experiment, it can be seen that there are significant differences regarding the free radicals contained in Fe(25)ZIF-8 and Fe(25)ZnO. It is concluded that the addition of trapping agent in Fe(25)ZIF-8 does not show a significant reduction compared with Fe(25)ZnO. The free radicals contained in Fe(25)ZIF-8 were not optimally able to degrade MB compared with the free radicals contained in Fe(25) ZnO. This result further confirms that the mesoporous structure is important properties to improve the photocatalytic performance which is in line with the FESEM results. The bulk structure of Fe(25)ZIF-8 causes a volume recombination which hinder the production of active species. Besides, the abundant of active species was caused by the lower recombination volume owing to the presence of mesoporous structure in Fe(25)ZnO. Furthermore the presence of n–n heterojunction system between two semiconductors (ZnO and α-Fe_2O_3) could also improve photocatalytic performance in Fe(25)ZnO.

Photocatalytic mechanism

The excellent photocatalytic activity was attributed to the effective charge separation and migration across the interface of Fe(25)ZnO. Thus, the photocatalytic mechanism of Fe(25)ZnO was illustrated in Fig. 15a. By referring to the characterization results of UV-vis DRS, it was found that the E_g values of ZnO and α-Fe_2O_3 were of 3.22 and 2.02 eV, respectively. Furthermore, the E_{CB} and E_{VB} was calculated based on eqn (5) and (6):[4]

$$E_{VB} = X - E^e + 0.5\,E_g \quad (5)$$

$$E_{CB} = E_{VB} - E_g \quad (6)$$

When, X is the absolute electronegativity of each semiconductor, which is ascribed the geometric mean of the absolute electronegativity of each constituent atom. The X value of ZnO and α-Fe_2O_3 are 5.75 and 5.88 eV, respectively.[40,74] E^e is the energy of free electrons on the hydrogen scale (~4.5 eV). E_g is ascribed the band gap energy of each the semiconductor. The E_{CB} and E_{VB} of ZnO are 0.36 and 2.86 eV, respectively. As for α-Fe_2O_3, the E_{CB} and E_{VB} are 0.37 and 2.39 eV, respectively.

α-Fe_2O_3 and ZnO are n-type semiconductor materials, where in n-type semiconductor the impurities are close to the CB. The addition of α-Fe_2O_3 to ZnO causes beneficial defects. When contact occurs, there will be a transfer of electrons from the Fermi level of ZnO to α-Fe_2O_3 until the Fermi level is equalized and creates an electric field that is effective for charge separation thus the CB α-Fe_2O_3 higher than that of CB ZnO.[75,76] Therefore, transfer electron was occurred from CB α-Fe_2O_3 to CB ZnO while the hole was remained in VB α-Fe_2O_3. The transfer of electron from CB α-Fe_2O_3 to ZnO was followed by reduced O_2 to radical ˙O_2^-. On the other hand, the holes in the VB ZnO oxidized the H_2O into a radical ˙OH, as a result of the E_{VB} value of ZnO (2.86 eV) more positive than the potential value of H_2O/˙OH (2.34 eV) based on eqn (5).

The proposed degradation process steps are:

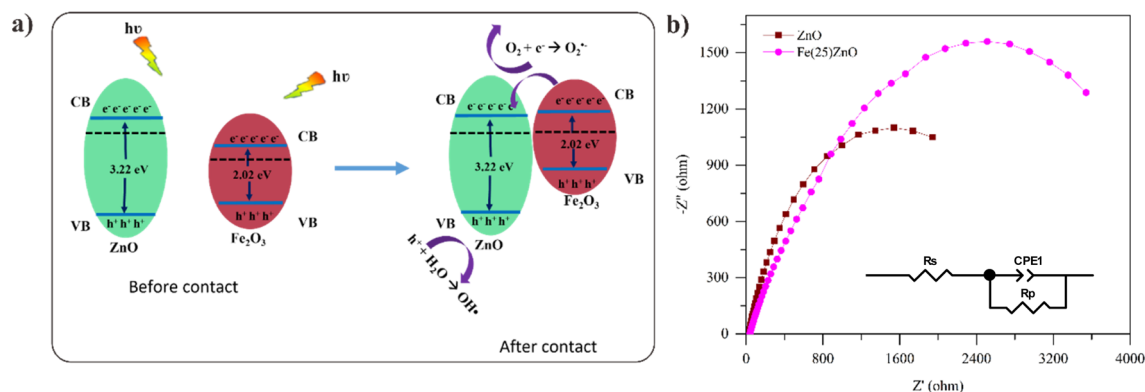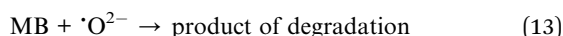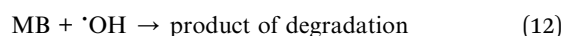$$Fe(25)ZnO + h\nu \rightarrow h^+ + e^- \quad (7)$$

$$H_2O + h^+ \rightarrow ˙OH + H^+ \quad (8)$$

$$O_2 + e^- \rightarrow ˙O^{2-} \quad (9)$$

$$˙O^{2-} + 2H^+ \rightarrow H_2O_2 \quad (10)$$

$$H_2O_2 \rightarrow 2\,˙OH \quad (11)$$

$$MB + ˙OH \rightarrow product\ of\ degradation \quad (12)$$

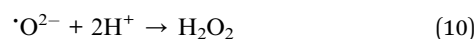$$MB + ˙O^{2-} \rightarrow product\ of\ degradation \quad (13)$$
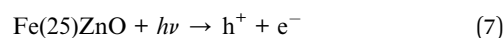
Fig. 15 (a) Possible mechanism for photocatalytic activity of Fe(25)ZnO (b) EIS spectra.

$$MB + h^+ \rightarrow \text{product of degradation} \qquad (14)$$

$$MB + e^- \rightarrow \text{product of degradation} \qquad (15)$$
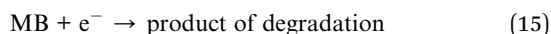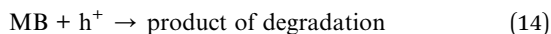
EIS analysis was performed to further investigate the charge carriers transfer in ZnO and Fe(25)ZnO.

As presented in Fig. 15b, ZnO shows a smaller arc radius compared to Fe(25)ZnO. A smaller arc radius suggests the more efficient charge transfer capability, which further facilitate the separation of charge carriers.[77] Further analysis over the Nyquist plots resulted in the fitted circuit and the corresponding R_s, R_{CT} and CPE values as tabulated in Table 8.

The CPE values are 0.80 and 0.67 for ZnO and Fe(25)ZnO, respectively, which indicates the nature of pseudocapacitor for both material. Meanwhile, the R represents the resistance, either the resistance from the solution (R_s) or charge transfer resistance (R_{CT}) within materials.[3,5] For both R_s and R_{CT}, ZnO shows lower values compared to Fe(25)ZnO, which indicates the

lower resistance in ZnO. However, we may note that the discrepancies in R_{CT} values of ZnO and Fe(25)ZnO is much higher than in R_s values, which suggest that the charge transfer resistance play a more significant role at determining the total resistance in ZnO and Fe(25)ZnO. Meanwhile, Based on PL spectra Fe(25)ZnO shows a better suppression of charge carriers' recombination than ZnO. Actually, the Fe(25)ZnO has superior photocatalytic performance than pristine ZnO caused by differences of morphology. As presented in the FESEM results in Fig. 4b and d, Fe(25)ZnO has porous morphology while the pristine ZnO shows more bulky structure. The porous morphology can be beneficial for the charge separation efficiency since the photogenerated electron and holes can easily reach the photocatalyst surface to contact with the reactant molecules. In contrast, in the bulk morphology, as is ZnO, the photogenerated electron and holes need a longer pathway to reach the photocatalyst surface, which increases the occurrence of the volume recombination.[78] Therefore, despite the lower charge transfer resistance in ZnO, this material shows an inferior performance compared to Fe(25)ZnO due to the volume recombination.

Reusability and stability

The stability of the photocatalyst is also vital performance variable for practical applications. The recycling test of Fe(25) ZIF-8 and Fe(25)ZnO was investigated to reveal the stability

Table 8 R_s, R_{CT} and CPE value of ZnO and Fe(25)ZnO

Material	R_s (ohm)	R_{CT} (ohm)	CPE
ZnO	31.4	3013	0.8
Fe(25)ZnO	38.64	5181	0.67
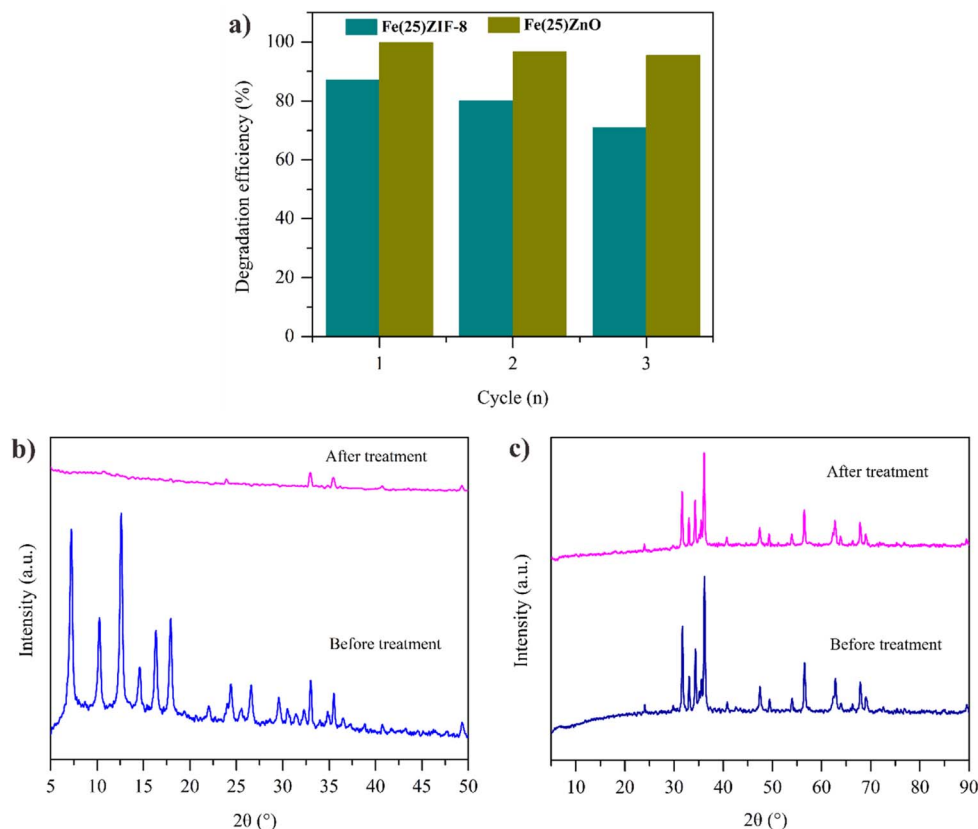
Fig. 16 (a) Reusability of Fe(25)ZIF-8 and Fe(25)ZnO for degradation of MB in solution (b) XRD pattern before and after recycle of Fe(25)ZIF-8 (c) XRD pattern before and after recycle of Fe(25)ZnO.

after several degradation in MB solution. Before recycling test, Fe(25)ZIF-8 and Fe(25)ZnO was collected from the MB solution by means of centrifugation then washed with methanol and ethanol several times, dried and applied in the next reactions.[79] The reusability of Fe(25)ZnO was better than Fe(25)ZIF-8 after three successive cycles (Fig. 16a). It was exhibited that the degradation efficiency of Fe(25)ZnO remained at higher than 95%, however the degradation efficiency of Fe(25)ZIF-8 was decreased until 70%. After recycling, Fe(25)ZIF-8 and Fe(25)ZnO were characterized by XRD as shown in Fig. 16b and c to determine the structure changes. There were no new diffraction peaks and characteristic peaks of Fe(25)ZnO still maintained after recycling (Fig. 16c), meanwhile the characteristic peak of Fe(25)ZIF-8 was not seen in the diffractogram after treatment (Fig. 16b). Thus, MOF-derived metal oxide composites have better photodegradation activity and stability than MOF composites which correlate with the presence of mesoporous heterojunction.

Conclusions

In summary, mesoporous heterojunction α-Fe$_2$O$_3$/ZnO composites were successfully prepared by simply calcination of α-Fe$_2$O$_3$/ZIF-8. The as-prepared Fe(25)ZIF-8 and Fe(25)ZnO exhibit spherical morphology with high and low density, respectively. α-Fe$_2$O$_3$/ZnO composites demonstrate a more effective photocatalytic performance of MB degradation than α-Fe$_2$O$_3$/ZIF-8 composites. The kinetic experiments confirmed that the photocatalytic process followed first order model. The photocatalytic rate of Fe(25)ZnO was 0.0347 min^{-1}, which was about 4.7 fold than pristine ZIF-8. The photocatalytic enhancement of MB over Fe(25)ZnO could be attributed to synergistic effect between mesoporous structure with n–n heterojunction system providing the chance for better MB adsorption and minimize the charge of volume recombination. In addition, the trapping experiment showed that hole and ˙OH are the main active species.

Conflicts of interest

There are no conflicts to declare.

Acknowledgements

Notes and references

1 F. Achouri, S. Corbel, A. Aboulaich, L. Balan, A. Ghrabi, M. Ben Said and R. Schneider, *J. Phys. Chem. Solids*, 2014, **75**, 1081–1087.

2 P. Dhiman, A. Kumar, M. Shekh, G. Sharma, G. Rana, D. V. N. Vo, N. AlMasoud, M. Naushad and Z. A. ALOthman, *Environ. Res.*, 2021, **197**, 111074.

3 Y. Liu, L. Sun, J. Wu, T. Fang, R. Cai and A. Wei, *Mater. Sci. Eng. B: Solid-State Mater. Adv. Technol.*, 2015, **194**, 9–13.

4 R. Subagyo, H. Tehubijuluw, W. Prasetyo Utomo, H. Dwi Rizqi, Y. Kusumawati, H. Bahruji and D. Prasetyoko, *Arabian J. Chem.*, 2022, **15**, 103754.

5 B. Tatykayev, F. Donat, H. Alem, L. Balan, G. Medjahdi, B. Uralbekov and R. Schneider, *ACS Omega*, 2017, **2**, 4946–4954.

6 S. Huang, J. Zhao, C. Wu, X. Wang, S. Fei, Q. Zhang, Q. Wang, Z. Chen, K. Uvdal and Z. Hu, *Chem. Eng. Sci.*, 2019, **209**, 115185.

7 T. T. Minh, N. T. T. Tu, T. T. Van Thi, L. T. Hoa, H. T. Long, N. H. Phong, T. L. M. Pham and D. Q. Khieu, *J. Nanomater.*, 2019, **2019**, 5198045.

8 S. Bazazi, N. Arsalani, A. Khataee and A. Goljanian, *J. Ind. Eng. Chem.*, 2018, **62**, 265–272.

9 S. Payra, S. Challagulla, Y. Bobde, C. Chakraborty, B. Ghosh and S. Roy, *J. Hazard. Mater.*, 2019, **373**, 377–388.

10 A. Faraji, N. Mehrdadi, N. M. Mahmoodi, M. Baghdadi and A. Pardakhti, *J. Mol. Struct.*, 2020, **1223**, 129028.

11 T. Luttrell, S. Halpegamage, J. Tao, A. Kramer, E. Sutter and M. Batzill, *Sci. Rep.*, 2015, **4**, 1–8.

12 Z. Gu, B. Zhang, Y. Asakura, S. Tsukuda, H. Kato, M. Kakihana and S. Yin, *Appl. Surf. Sci.*, 2020, **521**, 146213.

13 F. Mu, B. Dai, W. Zhao, L. Zhang, J. Xu and X. Guo, *Chin. Chem. Lett.*, 2020, **31**, 1773–1781.

14 A. A. Fauzi, A. A. Jalil, N. S. Hassan, F. F. A. Aziz, M. S. Azami, I. Hussain, R. Saravanan and D. N. Vo, *Chemosphere*, 2021, **286**, 131651.

15 Q. Wei, J. Sun, P. Song, J. Li, Z. Yang and Q. Wang, *Sens. Actuators, B*, 2020, **317**, 128205.

16 R. X. Chen, S. L. Zhu, J. Mao, Z. D. Cui, X. J. Yang, Y. Q. Liang and Z. Y. Li, *Int. J. Photoenergy*, 2015, **2015**, 183468.

17 R. Lei, H. Ni, R. Chen, B. Zhang, W. Zhan and Y. Li, *Chem. Phys. Lett.*, 2017, **673**, 1–6.

18 A. Bouziani, J. Park and A. Ozturk, *J. Photochem. Photobiol., A*, 2020, **400**, 112718.

19 L. Chen, H. F. Wang, C. Li and Q. Xu, *Chem. Sci.*, 2020, **11**, 5369–5403.

20 Y. Wang, X. Liu, L. Guo, L. Shang, S. Ge, G. Song, N. Naik, Q. Shao, J. Lin and Z. Guo, *J. Colloid Interface Sci.*, 2021, **599**, 566–576.

21 G. Peña-Velasco, L. Hinojosa-Reyes, G. A. Morán-Quintanilla, A. Hernández-Ramírez, M. Villanueva-Rodríguez and J. L. Guzmán-Mar, *Ceram. Int.*, 2021, **47**, 24632–24640.

22 J. Zheng, L. Sun, C. Jiao, Q. Shao, J. Lin, D. Pan, N. Naik and Z. Guo, *Colloids Surf., A*, 2021, **623**, 126629.

23 Y. Zhang, J. Zhou, X. Chen, Q. Feng and W. Cai, *J. Alloys Compd.*, 2019, **777**, 109–118.

24 J. Xu, S. Liu and Y. Liu, *RSC Adv.*, 2016, **6**, 52137–52142.

25 J. Xu, J. Gao, Y. Liu, Q. Li and L. Wang, *Mater. Res. Bull.*, 2017, **91**, 1–8.

26 X. Yang, L. Qiu and X. Luo, *RSC Adv.*, 2018, **8**, 4890–4894.

27 P. Zhu, X. Yin, X. Gao, G. Dong, J. Xu and C. Wang, *Chin. J. Catal.*, 2020, **42**, 175–183.

28 K. C. Devarayapalli, S. V. P. Vattikuti, K. S. Yoo, P. C. Nagajyothi and J. Shim, *J. Electroanal. Chem.*, 2020, **878**, 114634.

29 E. Santoso, R. Ediati, Z. Istiqomah, D. O. Sulistiono, R. E. Nugraha, Y. Kusumawati, H. Bahruji and D. Prasetyoko, *Microporous Mesoporous Mater.*, 2021, **310**, 110620.

30 P. Hu, C. Chen, J. Song and Z. Tang, *Mater. Sci. Semicond. Process.*, 2018, **77**, 40–49.

31 N. Mostafa Marzouk, A. O. Abo El Naga, S. A. Younis, S. A. Shaban, A. M. El Torgoman and F. Y. El Kady, *J. Environ. Chem. Eng.*, 2021, **9**, 105035.

32 P. Liang, C. Zhang, H. Sun, S. Liu, M. Tadé and S. Wang, *RSC Adv.*, 2016, **6**, 95903–95909.

33 N. M. Mahmoodi, S. Keshavarzi, M. Oveisi, S. Rahimi and B. Hayati, *J. Mol. Liq.*, 2019, **291**, 111333.

34 A. Anžlovar, Z. Crnjak Orel, K. Kogej and M. Žigon, *J. Nanomater.*, 2012, **2012**, 760872.

35 M. S. Azmina, R. M. Nor, H. A. Rafaie, N. S. A. Razak, S. F. A. Sani and Z. Osman, *Appl. Nanosci.*, 2017, **7**, 885–892.

36 R. M. Mohamed and A. Shawky, *Opt. Mater.*, 2022, **124**, 112012.

37 J. Abdi, N. M. Mahmoodi, M. Vossoughi and I. Alemzadeh, *Microporous Mesoporous Mater.*, 2019, **273**, 177–188.

38 W. S. Chiu, P. S. Khiew, M. Cloke, D. Isa, T. K. Tan, S. Radiman, R. Abd-Shukor, M. A. A. Hamid, N. M. Huang, H. N. Lim and C. H. Chia, *Chem. Eng. J.*, 2010, **158**, 345–352.

39 D. A. Ali, E. E. El-Katori and E. A. Kasim, *Z. Phys. Chem.*, 2021, **235**, 239–263.

40 C. Chen, W. Bi, Z. Xia, W. Yuan and L. Li, *ACS Omega*, 2020, **5**, 13185–13195.

41 P. Nandi and D. Das, *Appl. Surf. Sci.*, 2019, **465**, 546–556.

42 Y. T. Prabhu, V. Navakoteswara Rao, M. V. Shankar, B. Sreedhar and U. Pal, *New J. Chem.*, 2019, **43**, 6794–6805.

43 A. Kubiak, S. Żółtowska, E. Gabała, M. Szybowicz, K. Siwińska-Ciesielczyk and T. Jesionowski, *Powder Technol.*, 2021, **386**, 221–235.

44 N. Chang, Y. R. Chen, F. Xie, Y. P. Liu and H. T. Wang, *Microporous Mesoporous Mater.*, 2020, **307**, 110530.

45 H. Kaur, G. C. Mohanta, V. Gupta, D. Kukkar and S. Tyagi, *J. Drug Delivery Sci. Technol.*, 2017, **41**, 106–112.

46 A. Chakraborty, D. A. Islam and H. Acharya, *J. Solid State Chem.*, 2019, **269**, 566–574.

47 N. A. Rodríguez, R. Parra and M. A. Grela, *SN Appl. Sci.*, 2020, **2**, 1–9.

48 D. K. L. Harijan, S. Gupta, S. K. Ben, A. Srivastava, J. Singh and V. Chandra, *Phys. B*, 2022, **627**, 413567.

49 M. Al-Haddad, A. Shawky and I. A. Mkhalid, *J. Taiwan Inst. Chem. Eng.*, 2021, **123**, 284–292.

50 N. M. Shooshtari and M. M. Ghazi, *Chem. Eng. J.*, 2017, **315**, 527–536.

51 P. Chamoli, R. K. Shukla, A. N. Bezbaruah, K. K. Kar and K. K. Raina, *Appl. Surf. Sci.*, 2021, **555**, 149663.

52 X. Zeng, L. Huang, C. Wang, J. Wang, J. Li and X. Luo, *ACS Appl. Mater. Interfaces*, 2016, **8**, 20274–20282.

53 Z. Ma, F. Ren, Y. Deng and A. A. Volinsky, *Optik*, 2020, **219**, 165204.

54 C. Liu, Y. Qiu, F. Wang, K. Wang, Q. Liang and Z. Chen, *Adv. Mater. Interfaces*, 2017, **4**, 1–11.

55 X. Cheng, S. Cao, Y. Huan, Z. Bai, M. Li, H. Wu, R. Zhang, W. Peng, Z. Ji and X. Yan, *Energy Technol.*, 2018, **7**, 1800899.

56 Y. Dong, T. Hu, M. Pudukudy, H. Su, L. Jiang, S. Shan and Q. Jia, *Mater. Chem. Phys.*, 2020, **251**, 123060.

57 A. Khandelwal, N. Narayanan, E. Varghese and S. Gupta, *Bull. Environ. Contam. Toxicol.*, 2020, **104**, 503–510.

58 H. Dai, X. Yuan, L. Jiang, H. Wang, J. Zhang and J. Zhang, *Coord. Chem. Rev.*, 2021, **441**, 213985.

59 W. Aulia, A. Ahnaf, M. Y. Irianto, R. Ediati, R. M. Iqbal, R. A. Rachman and U. T. I. Martia, *IPTEK J. Technol. Sci.*, 2020, **31**, 18.

60 L. A. Calzada, R. Castellanos, L. A. García and T. E. Klimova, *Microporous Mesoporous Mater.*, 2019, **285**, 247–258.

61 A. Chakraborty, D. A. Islam and H. Acharya, *J. Solid State Chem.*, 2019, **269**, 566–574.

62 S. S. Cui, X. Liu, Y. B. Shi, M. Y. Ding and X. F. Yang, *Rare Met.*, 2022, **41**, 2405–2416.

63 P. Y. Kuang, Y. Z. Su, G. F. Chen, Z. Luo, S. Y. Xing, N. Li and Z. Q. Liu, *Appl. Surf. Sci.*, 2015, **358**, 296–303.

64 S. Sun, M. Sun, Y. Kong, Y. Fang and Y. Yao, *J. Sol-Gel Sci. Technol.*, 2016, **80**, 719–727.

65 A. Norouzi and A. Nezamzadeh-Ejhieh, *Phys. B*, 2020, **599**, 412422.

66 J. Zhang, X. Xu, W. Zhang, Y. Huang and P. Zhang, *Spectrochim. Acta, Part A*, 2022, **274**, 121103.

67 Z. Yang, J. Zhang, W. Zhang, Q. Zhou, J. Shen and Y. Huang, *J. Clean. Prod.*, 2023, **382**, 135391.

68 G. Fan, J. Luo, L. Guo, R. Lin, X. Zheng and S. A. Snyder, *Chemosphere*, 2018, **209**, 44–52.

69 A. Sekar and R. Yadav, *Optik*, 2021, **242**, 167311.

70 P. Muhambihai, V. Rama and P. Subramaniam, *Environ. Nanotechnol., Monit. Manage.*, 2020, **14**, 100360.

71 X. H. Yi, F. X. Wang, X. D. Du, H. Fu and C. C. Wang, *Polyhedron*, 2018, **152**, 216–224.

72 E. Amdeha and R. S. Mohamed, *Environ. Technol.*, 2021, **42**, 842–859.

73 D. Tuncel and A. N. Ökte, *Catal. Today*, 2019, **328**, 149–156.

74 X. F. Cao, P. Yue, Q. R. Wei, Y. F. Dang, S. Q. Zhang, Z. X. Wei and R. Z. Wang, *J. Mater. Sci.*, 2021, **56**, 7862–7878.

75 L. G. da Trindade, G. Y. Hata, J. C. Souza, M. R. S. Soares, E. R. Leite, E. C. Pereira, E. Longo and T. M. Mazzo, *J. Mater. Sci.*, 2020, **55**, 2923–2936.

76 A. M. Tama, S. Das, S. Dutta, M. D. I. Bhuyan, M. N. Islam and M. A. Basith, *RSC Adv.*, 2019, **9**, 40357–40367.

77 W. P. Utomo, H. Wu and Y. H. Ng, *Small*, 2022, **18**, 2270131.

78 D. Hartanto, G. Yuhaneka, W. P. Utomo, A. I. Rozafia, Y. Kusumawati, W. Dahani and A. Iryani, *RSC Adv.*, 2022, **12**, 5665–5676.

79 A. R. P. Hidayat, D. O. Sulistiono, I. K. Murwani, B. F. Endrawati, H. Fansuri, L. L. Zulfa and R. Ediati, *J. Environ. Chem. Eng.*, 2021, **9**, 106675.